Proceedings of the ASME 2010 3rd Joint US-European Fluids Engineering Summer Meeting and 8th International Conference on Nanochannels, Microchannels, and Minichannels
FEDSM-ICNMM2010
August 1-5, 2010, Montreal, Canada

FEDSM-ICNMM2010-30861

FLUTTER INSTABILITY OF A FLUID-CONVEYING, FLUID-IMMERSED PIPE AFFIXED TO A RIGID BODY

Aren M. Hellum *
Ranjan Mukherjee
Department of Mechanical Engineering
Michigan State University
East Lansing, MI 48825
Email: hellumar@msu.edu

Andrew J. Hull
Advanced Acoustic Systems Division
Autonomous and Defensive Systems Department
Naval Undersea Warfare Center
Newport, RI 02841
email: andrew.hull@navy.mil

Abstract

Studies of fluid-conveying pipes typically consider systems with an anchor at one or more boundaries, such as pinning or clamping. These types of conditions are satisfactory in the study of many common engineering applications, such as pipelines or heat exhangers. However, a small, fish-like submersible propelled by a fluttering fluid-conveying pipe requires boundary conditions which account for the relative freedom at both ends of the pipe. A submersible of this type achieves its propulsion by a combination of jet action and thrust produced by the fluttering pipe. A simple model of this type of vehicle was devised, consisting of a rigid body affixed to a fluid-conveying pipe. The applicable linearized boundary conditions were derived, and this rigid-free case can be shown to be a generalization of both the free-free and cantilever conditions. The equation of motion of this rigid-free system approaches that of the cantilever and free-free systems for appropriately large and small rigid body masses, respectively. "Intermediate" values of (non-dimensional) rigid body mass, in the range corresponding to a proposed physical realization of the system, were investigated. Consistent with prior work, it was found that, with the addition of external flow generated by the forward motion of the submersible through still water, the onset of flutter instability can be achieved for lower values of conveyed (internal) velocity than would be required in the absence of external flow. Furthermore, the onset of flutter for certain rigid body masses can be achieved at a lower internal velocity than the cantilever case at the same external speed. This point is critical; since it is the internal velocity which must be "paid for", by powering the system's prime mover, reduction of the required velocity to achieve flutter has the potential to improve the submersible's efficiency.

1 Background

1.1 Fluid Conveying Pipes

The dynamics of fluid-conveying pipes have been well-studied in the literature, both with [2] [8] and without [7] external flow. In this section we will review the relevant equations for these systems, and provide one method of determining the onset of flutter instability. The equations of motion for a cantilever pipe conveying fluid with velocity U and immersed in inviscid fluid flowing with velocity U_e are as follows:

$$
\begin{aligned}
&EI\frac{\partial^4 y}{\partial x^4}+(MU^2+M_eU_e^2)\frac{\partial^2 y}{\partial x^2}\\
&+2(MU+M_eU_e)\frac{\partial^2 y}{\partial x\partial t}+(m+M+M_e)\frac{\partial^2 y}{\partial t^2}=0 \qquad (1)\\
&y(0,t)=0 \qquad \frac{\partial y}{\partial x}(0,t)=0\\
&\frac{\partial^2 y}{\partial x^2}(L,t)=0 \qquad \frac{\partial^3 y}{\partial x^3}(L,t)=0
\end{aligned}
$$

Here, $y(x,t)$ is the displacement of the pipe as shown in Figure

*Address all correspondence to this author.

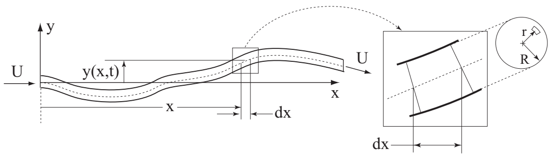

FIGURE 1. A fluid-conveying pipe, with a magnified view of a small length element.

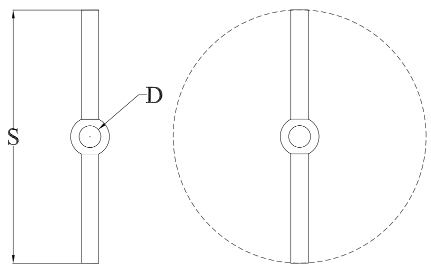

FIGURE 2. A finned tube arrangement, with internal fluid-conveying diameter D and tail span S. At right, surrounded by a dashed line, is the area responsible for the added external mass, equal to $\rho_{fl}\pi\frac{S^2}{4}L$, where ρ_{fl} is the density of the external fluid.

1. E, I, L represent the Young's modulus, area moment of inertia, and length of the pipe, respectively. m, M, M_e represent the mass per unit length of the beam, the internal (conveyed) fluid and the external fluid. The masses per unit length of the beam and internal fluid are straightforward, but the external fluid mass requires approximation. The added mass coefficient [10] can be used to approximate this mass. As one example, the added mass associated with a cylindrical beam is equal to the mass of water displaced by the cylinder. For thin cross sections, such as a flat plate, the added mass is equal to the mass of water within a cylinder which circumscribes the plate. A "finned tube" arrangement well suited to providing both a fluid conduit and a tail of adequate span is depicted in Figure 2, with the area responsible for added external mass marked. The authors note that Equation 1 is a simplified version of the equations of motion as presented in [8], ignoring gravitational, viscous, pressurization and tensile effects. Pressurization effects are negligible because we are modelling a submersible operating at depth and pumping water at that depth. Equation 1 may be non-dimensionalized via the following change of variables:

$$X = \frac{x}{L} \qquad Y = \frac{y}{L} \qquad T = \frac{t}{L^2}\left(\frac{EI}{m+M+M_e}\right)^{1/2} \tag{2}$$

We may define the non-dimensional velocities, u_i, u_e and the mass fractions β_i, β_e as follows

$$u_i = \left(\frac{M}{EI}\right)^{1/2} UL \qquad u_e = \left(\frac{M_e}{EI}\right)^{1/2} U_e L$$
$$\beta_i = \left(\frac{M}{m+M+M_e}\right) \qquad \beta_e = \left(\frac{M_e}{m+M+M_e}\right)$$

Equation 1 may now be written in its non-dimensional form,

$$\begin{aligned}&\frac{\partial^4 Y}{\partial X^4} + (u_i^2 + u_e^2)\frac{\partial^2 Y}{\partial X^2} \\ &+ 2\left(\beta_i^{1/2}u_i + \beta_e^{1/2}u_e\right)\frac{\partial^2 Y}{\partial X \partial T} + \frac{\partial^2 Y}{\partial T^2} = 0\end{aligned} \tag{3}$$

If a separable form is assumed for $y(x,t)$ such that $y(x,t) = f(x)e^{i\Omega t}$, the above yields the equivalent nondimensional expression

$$Y(X,T) = \phi(X)e^{i\omega T} \tag{4}$$

where the nondimensional frequency, ω is defined as:

$$\omega = \left(\frac{m+M+M_e}{EI}\right)^{1/2}\Omega L^2$$

Separation yields the ordinary differential equation and boundary conditions

$$\begin{aligned}&\frac{d^4\phi}{dX^4} + (u_i^2+u_e^2)\frac{d^2\phi}{dX^2} + 2\left(\beta_i u_i + \beta_e u_e\right) i\omega\frac{d\phi}{dX} \\ &-\omega^2\phi = 0 \\ &\phi(0) = 0 \qquad \phi'(0) = 0 \\ &\phi''(1) = 0 \qquad \phi'''(1) = 0\end{aligned} \tag{5}$$

The solution ϕ is assumed to be of the form $\phi(X) = Ae^{zX}$. For specific values of u_i, u_e, β_i, β_e, the characteristic polynomial of Equation 5 provides four roots z_n, where $z_n = z_n(\omega)$. The solution of $\phi(X)$ therefore takes the form

$$\phi(X) = A_1e^{z_1X} + A_2e^{z_2X} + A_3e^{z_3X} + A_4e^{z_4X} \tag{6}$$

Substitution of Equation 6 into Equation 5 yields the identity

$$\underbrace{\begin{bmatrix} 1 & 1 & 1 & 1 \\ z_1 & z_2 & z_3 & z_4 \\ z_1^2e^{z_1} & z_2^2e^{z_2} & z_3^2e^{z_3} & z_4^2e^{z_4} \\ z_1^3e^{z_1} & z_2^3e^{z_2} & z_3^3e^{z_3} & z_4^3e^{z_4}\end{bmatrix}}_{\mathbf{Z}} \underbrace{\begin{bmatrix} A_1 \\ A_2 \\ A_3 \\ A_4\end{bmatrix}}_{\mathbf{A}} = \underbrace{\begin{bmatrix} 0 \\ 0 \\ 0 \\ 0\end{bmatrix}}_{\mathbf{0}} \tag{7}$$

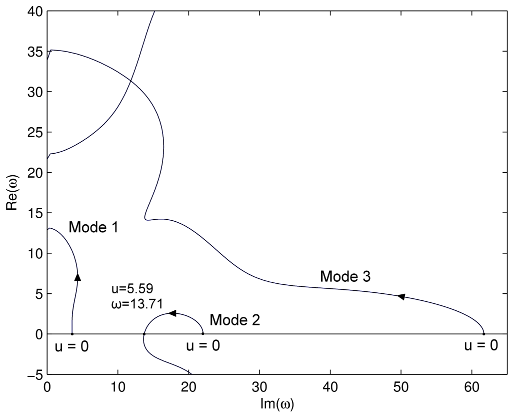

FIGURE 3. Argand diagram of the first three modes of a fluttering cantilever pipe, $\beta_i = 0.2,\ \beta_e = 0$.

A non-trivial solution (for ω) of Equation 7 is obtained by numerical evaluation of the roots of $Det(\mathbf{Z}) = 0$. This equation has infinite roots in ω. The real and imaginary parts the first three roots are plotted in Figure 3 for $\beta_i = 0.2,\ \beta_e = 0$. This figure, called an Argand diagram, is composed of three branches, each one the locus of a vibrational mode. These loci are formed by first obtaining the real root of each mode at $u_i = 0$, which match those of a regular, non fluid conveying cantilever beam, then finding ω numerically as u is slowly increased. The onset of flutter instability in mode two is marked in Figure 3 where its locus crosses the imaginary axis. Substitution of Equation 6 into Equation 4 yields

$$
\begin{aligned}
Y(X,T) &= \sum_{n=1}^{4} A_n e^{z_n X} e^{i\omega T} \\
&= \sum_{n=1}^{4} A_n \underbrace{e^{Re[z_n]X}}_{(i)} \underbrace{e^{i(Im[z_n]X + Re[\omega]T)}}_{(ii)} \underbrace{e^{-Im[\omega]T}}_{(iii)}
\end{aligned} \tag{8}
$$

$Y(X,T)$ is a product of three exponential terms of which the first term is bounded (since X is bounded), and the second term is periodic since the exponent is imaginary. The third term is unbounded with time if $Im[\omega] < 0$; if $Re[\omega] > 0$, this represents the onset of flutter instability. The mode and velocity at which the pipe becomes unstable depends on the fluid mass fractions $\beta_i,\ \beta_e$. Though not necessary for determining the natural frequency (ω) and wavenumbers (z_n) of the system, the coefficients A_n may be determined by computing the nullspace of the matrix $\mathbf{Z}$ in Equation 7, once $\omega,\ z_n$ have been determined. These coefficients are needed to estimate the force exerted by the beam on the surrounding fluid, discussed presently.

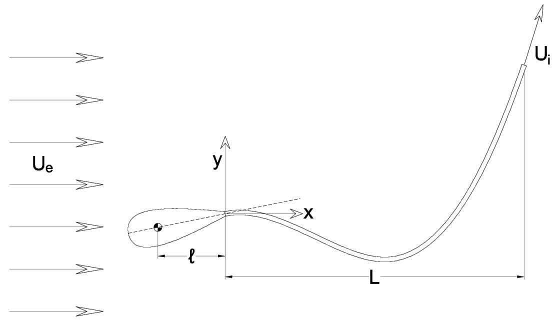

FIGURE 4. The proposed submersible. The linearized form of the equations of motion means that $\ell,\ L$ are constants, not related to $y(x,t)$.

1.2 Motivation

Fish-like propulsion has been a topic of interest in the academic community for more than 60 years, and several robotic platforms have been built (see [11]) to exploit the phenomenon. The combined mechanism proposed here (Figure 4), in which a fluttering fluid-conveying pipe provides thrust by both tail and jet action, has also been implemented. That system, constructed in the mid-1970's by Paidoussis [5], was found to produce positive thrust only if the phase velocity of the tail displacement was greater than the forward speed of the vessel. That work and the accompanying patent [6] are primarily experimental in nature, and contain a variety of construction details for their system, as well as the thrust optimizations performed.

Thrust production via a high phase velocity traveling wave was described first in an early paper by Lighthill [4], which used slender body analysis to approximate the thrust produced by an idealized fish. Lighthill found that a traveling waveform, for example $y(x,t) = f(x)\cos(kx + \Omega t)$, with phase velocity $P = \Omega/k$, may be used to propel a body at some speed U, where $P > U$. As the reader is no doubt aware, Equation 8 is the sum of four traveling waveforms. Per the predictions of Lighthill, a waveform with dimensional wavenumber and frequency $Z_n,\ \Omega$ will only have positive thrust if

$$\frac{P_n}{U_e} > 1 \qquad or \qquad \frac{\Omega/Z_n}{U_e} > 1$$

This dimensional constraint is equivalent to the non-dimensional requirement that

$$\frac{\omega}{z_n} > \frac{u_e}{\beta^{1/2}} \tag{9}$$

where ω/z_n is the waveform's non-dimensional phase velocity.

The system described by Paidoussis in [9] is described colloquially in that work to have a (single) phase velocity while operating, which was measured by direct observation. While simple to determine experimentally, determination of positive thrust by the phase velocity is not straightforward in the context of Equation 8 in that four traveling waveforms of different, spatially variable amplitudes and phase velocities are propagating down the pipe. It is easier to estimate the thrust by the method laid out by both Lighthill [4] and Wu [12]. In those papers, a slender[1] fish is considered, and has displacement from its neutral position equal to $y(x,t)$. The time-averaged thrust $\overline{\tau}$ provided by this displacement is given as:

$$\overline{\tau} = \frac{1}{2}M_e\left(\overline{[\dot{y}^2 - U_e y'^2]}_{x=L} - \overline{[\dot{y}^2 - U_e y'^2]}_{x=0}\right) \tag{10}$$

In Equation 10, the overbar refers to a time average over a long time. Both Lighthill and Wu derive the expression without the assumption of harmonic motion; if harmonic motion is assumed, the time average over a single cycle is sufficient. Note that Equation 10 differs slightly from that found in [12][2]. Wu's assumption that no mass is affected at $x = 0$ is relaxed, since we are dealing with a uniform tail, rather than a tapered fish which has zero area at the tip.

A similar expression is derived for the average power $\overline{P}$ required to provide the displacements $y(x,t)$. This expression includes the power required to generate the vortex wake, into which energy is shed.

$$\overline{P} = U_e M_e\left(\overline{[\dot{y}(\dot{y}+U_e y')]}_{x=L} - \overline{[\dot{y}(\dot{y}+U_e y')]}_{x=0}\right) \tag{11}$$

Equations 10 and 11 may be used to form a definition for hydrodynamic efficiency of the tail's motions:

$$\eta = \frac{\overline{\tau}U_e}{\overline{P}} \tag{12}$$

Note that this efficiency does not account for power lost to internal fluid shearing in the jet, or external drag. The submersible's total efficiency will therefore be somewhat lower after these effects are accounted for.

Analysis of the submersible device proposed here requires the use of the rigid body boundary condition developed in Section 2.1. This device, depicted conceptually in Figure 4 has a hull much smaller than that of the surface vessel used by Paidoussis [9]. This reduced size and mass requires that the dynamics of the hull be accounted for in modeling the dynamics of the tail-like pipe. A surface vessel does not have a unique relationship between the vessel's displacement and weight, only requiring that it have positive buoyancy, whereas a neutrally-buoyant submersible requires a reduced mass if it is to have a smaller displacement. A smaller displacement leads to lower drag and increased maneuverability. While this proposed device is perhaps a less "pure" example of fish-like propulsion than other platforms, it offers many of the same advantages, including noise reduction and the ability to safely work near human divers and animals. We believe that similar handling characteristics can also be realized by controlling the flow rate of the conveyed fluid, though this is beyond the scope of this communication.

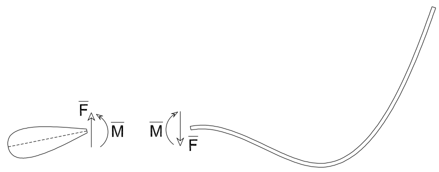

FIGURE 5. Rigid body boundary conditions.

2 Fluid Conveying Rigid Body-Free Pipe
2.1 Boundary conditions

The linearized boundary conditions for a rigid body at $x = 0$ are:

$$EI\frac{\partial^3 y}{\partial x^3} + M_B\left(\frac{\partial^2 y}{\partial t^2} - \ell\frac{\partial^3 y}{\partial x \partial t^2}\right) = 0 \tag{13a}$$

$$EI\frac{\partial^2 y}{\partial x^2} + (J_0 + M_B\ell^2)\frac{\partial^3 y}{\partial x \partial t^2} - M_B\ell\frac{\partial^2 y}{\partial t^2} = 0 \tag{13b}$$

In Equation 13, M_B refers to the mass of the rigid body, J_0 is the moment of inertia of the rigid body about the point $x = 0$, and ℓ is the distance between the origin and the center of mass of the rigid body. The boundary conditions above are similar to those found by Rama Bhat and Wagner in [1], with the exception that they have been derived at $x = 0$ rather than $x = L$. Some simplifications have been made to obtain Equation 13. First, the expressions have been linearized, such that $\sin\theta \approx \partial y(0)/\partial x$, where θ is the angle between the rigid body and the x-axis. Note that this linearization does not impose additional restriction beyond that required of the Euler-Bernoulli beam model. A more subtle simplification lies in ignoring the effect of the external fluid velocity on the dynamics of the rigid body. While the added mass of the surrounding fluid may be accounted for by increasing M_B and J_0, terms analogous to the y_{xx}, y_{xt} terms from Equation 1

[1] A good description of the meaning of "slender" as used here may be found in §2 of Wu [12].

[2] Equation (47) in that work)

are not present, and may be appropriate. A much more detailed version of the equations of motion for a submersible is derived in [3], which accounts for acceleration in x and θ, as well as a detailed accounting of external fluid and many other effects. The equations presented in that work, however, are not analytically tractable. Equation 2 may be applied to Equation 13 to obtain the following non-dimensional expressions:

$$Y''' + \mu(\ddot{Y} - \lambda\ddot{Y}') = 0 \quad (14a)$$

$$Y'' + \mu[(\psi_J + \lambda^2)\ddot{Y}' - \lambda\ddot{Y}] = 0 \quad (14b)$$

In Equation 14,

$$\mu = \frac{M_B}{(m+M+M_e)L} \qquad \lambda = \frac{\ell}{L} \qquad \psi_J = \frac{J_0}{M_B L^2} \quad (15)$$

Physically, μ is the mass ratio between the body and the rest of the system, λ non-dimensionalizes the length, and ψ_J accounts for the shape of the rigid body. Note that as μ approaches 0, Equation 14 approaches the expressions for a free end, while as μ approaches ∞, the equations approach the expressions for a clamped end. The former point is trivial; to clarify the latter, Equation 14 is rewritten below in the limit as μ goes to ∞, and quantities shared by all terms are removed:

$$(\ddot{Y} - \lambda\ddot{Y}') = 0$$

$$[(\psi_J + \lambda^2)\ddot{Y}' - \lambda\ddot{Y}] = 0$$

Therefore

$$(\psi_J + \lambda^2)\ddot{Y}' = \lambda^2\ddot{Y}'$$

This requires that

$$\ddot{Y}' = 0 \quad \text{or} \quad \psi_J = 0$$

The condition $\psi_J = 0$ is impossible for a body of finite size, so the former condition must hold. The zero acceleration condition for a clamped end now follows trivially.

2.2 Method of Analysis

The equations of motion for the rigid body-free boundary condition are approached in the same way as those for the cantilever, though Equation 7 is replaced by an equivalent statement for the new boundary conditions, shown below:

$$\underbrace{\begin{bmatrix} \eta_1 & \eta_2 & \eta_3 & \eta_4 \\ \zeta_1 & \zeta_2 & \zeta_3 & \zeta_4 \\ z_1^2 e^{z_1} & z_2^2 e^{z_2} & z_3^2 e^{z_3} & z_4^2 e^{z_4} \\ z_1^3 e^{z_1} & z_2^3 e^{z_2} & z_3^3 e^{z_3} & z_4^3 e^{z_4} \end{bmatrix}}_{\mathbf{Z}} \underbrace{\begin{bmatrix} A_1 \\ A_2 \\ A_3 \\ A_4 \end{bmatrix}}_{\mathbf{A}} = \underbrace{\begin{bmatrix} 0 \\ 0 \\ 0 \\ 0 \end{bmatrix}}_{\mathbf{0}} \quad (17)$$

In Equation 17, η_n, ζ_n are the moment and shear boundary conditions found in Equation 14 such that

$$\eta_n = z_n^2 - \mu\omega^2((\psi + \lambda^2)z_n - \lambda)$$

$$\zeta_n = z_n^3 - \mu\omega^2(1 - \lambda z_n)$$

The proposed application, that of a fish-like submersible swimming with reasonably constant forward speed, requires that the oscillations of the fluttering tail do not grow in time. The points of neutral stability ($Im[\omega] = 0$) are therefore sought in the u_i, u_e parameter space. While it would be possible to determine these curves by repeated examination of Argand diagrams like Figure 3, the number of points required to obtain a curve with high resolution renders this method prohibitively time-expensive. An automated method, similar in character to that used to build the Argand diagram, is therefore proposed.

First, the u_i required for neutral stability at $u_e = 0$ is computed by interpolating values of u_i with the property $Im[\omega] \approx 0$. This is repeated for $u_e = \Delta$, where Δ is a small number. Subsequent points may be found by extrapolating at a distance of Δ from the last point to obtain a guess for the neutrally stable u_i, u_e, then iterating near that guess. The "direction" of iteration is important in this procedure; simply iterating in u_i or u_e will fail in some regions of the parameter space. Iterating perpendicular to the guessed direction of the curve was found to give good results. A curve with sharper turns will require a lower value of Δ to achieve good results; the lowest value required to compute the curves in the current work was 0.02, with a velocity iteration stepsize of 0.002. This velocity iteration stepsize was kept constant, even when Δ was increased, to minimize interpolation error. Figure 6 is provided to illustrate the algorithm.

3 Dynamics and Applications

3.1 Stability in μ-space

The stability of the fluid conveying pipe with rigid body-free boundary conditions was assessed in the u_i u_e space for various values of μ, using mass ratios $\beta_i = 0.01$, $\beta_e = 0.9$. The extreme values for β are the product of a proposed implementation of the submersible discussed in Section 1.2. In particular, the large value of β_e is due to the use of a high-aspect ratio finned tube

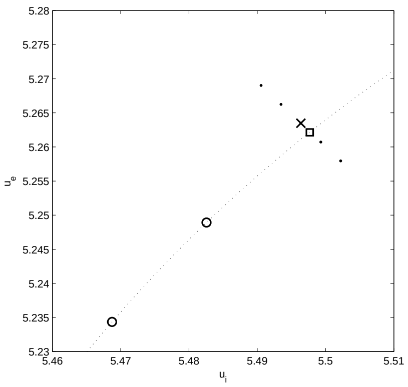

FIGURE 6. Finding the curve of neutral stability. The two known points are marked with ○, the guess point with a ×, and the point found with a □. The iteration points include the guess point, and four others, marked by •. The dotted line depicts the curve, which is not known *a priori*.

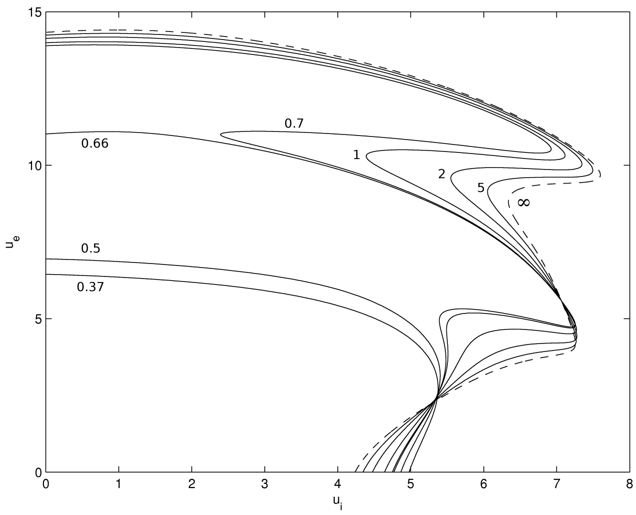

FIGURE 7. Curves of neutral stability for various values of μ. The dashed line indicates the cantilever boundary condition, $\mu = \infty$. The curves depict $\mu = \infty,\ 5,\ 2,\ 1,\ 0.7,\ 0.66,\ 0.5,\ 0.37$.

(Figure 2) as the pipe. Rigid body parameters $\psi_J = 1/3$, $\lambda = 1/3$ were used. These values correspond to a uniform cylinder with length two-thirds that of the pipe.

Curves of neutral stability are depicted in Figure 7. For each curve, the area inside the curve (toward the origin) is stable, and the area outside is unstable. Each curve was determined by first finding the u_i required to create flutter instability at $u_e = 0$. u_e and u_i are then perturbed along the predicted direction of the curve, and the nearby point of neutral stability can be found. This method of using nearby points on the curve is employed to reduce

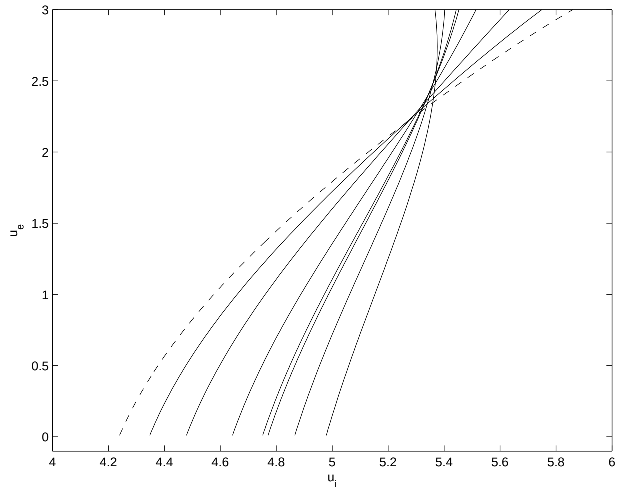

FIGURE 8. Curves of neutral stability for various values of μ at low values of u_e. Note the proximity of all curves near the point $u_i = 5.3,\ u_e = 2.5$. For $u_e < 2.5$, the curves depict, from left to right, $\mu = \infty,\ 5,\ 2,\ 1,\ 0.7,\ 0.66,\ 0.5,\ 0.37$.

the search space, and to make sure that the algorithm used to find ω has a starting guess sufficiently close to the desired root.

The difference between the low-μ and high-μ curves in Figure 7 is quite striking, considering the relatively small difference in critical u_i at $u_e = 0$. At low u_e, the u_i required to create flutter instability decreases with increased μ, until approximately $u_i = 5.3,\ u_e = 2.5$. The proximity of all curves to this point is interesting, but the authors see no theoretical reason for this confluence. A closeup view of this region is given as Figure 8. For values of $u_e > 2.5$, the curves diverge. In general, lower values of μ require a lower u_i at a given u_e to achieve flutter instability. This trend is most apparent for $\mu \leq 0.66$. The "kink" in the curves for $\mu > 0.5$ may be explained by reference to Figure 9. Higher mass ratios undergo one or more sharp jumps in natural frequency as u_e increases.

3.2 Thrust characteristics

Equation 10 may be non-dimensionalized, and the average over one cycle computed, to give the average non-dimensional thrust τ^*.

$$\tau^* = \frac{\overline{\tau}L^2}{EI} = \frac{\omega_{cr}}{4\pi}\int_0^{\frac{2\pi}{\omega_{cr}}} \Big(\left[\dot{Y}^2\beta_e - u_e^2 Y'^2\right]_{X=1} - \left[\dot{Y}^2\beta_e - u_e^2 Y'^2\right]_{X=0} \Big) dT \tag{18}$$

The function $Y(X,T)$ is found by the method laid out in Section 1.1, and takes the form of Equation 8. Equation 8 has both real

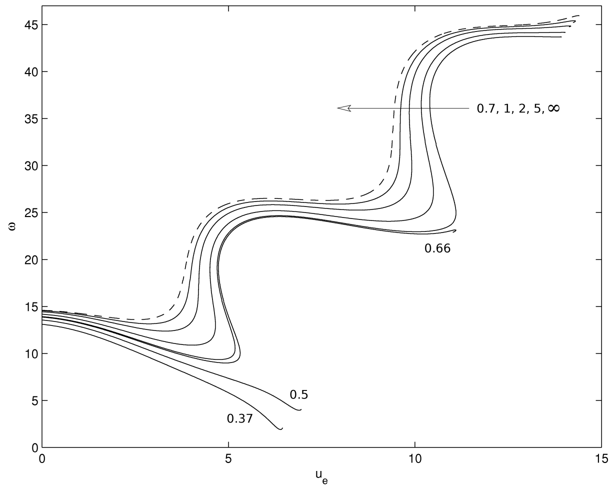

FIGURE 9. Critical frequency, ω_{cr}, as a function of u_e.

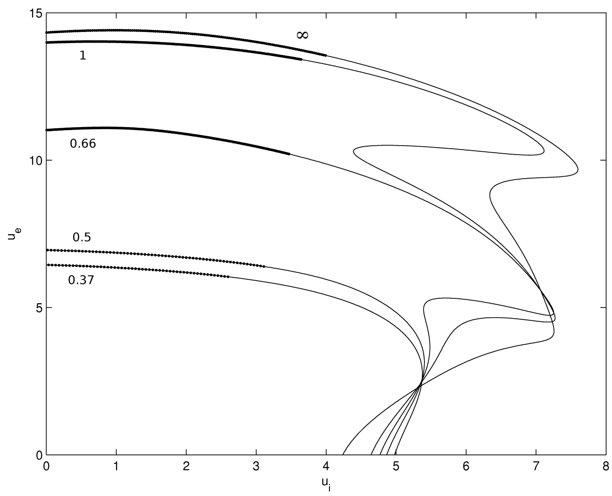

FIGURE 10. Curves of neutral stability for $\mu = 0.37,\ 0.5,\ 0.66,\ 1,\ \infty$. The thickened portion of each curve depicts the region of negative thrust.

and imaginary parts; only the real part is physically manifest, and contributes to the thrust. Assuming neutral stability ($Im[\omega] = 0$), the real part of Equation 8 is

$$Y(X,T) = \sum_{n=1}^{4} e^{Re[z_n]X} \times \left(Re[A_n]\cos(Im[z_n]X + Re[\omega]T) - Im[A_n]\sin(Im[z_n]X + Re[\omega]T) \right) \tag{19}$$

The coefficients A_n in Equations 8 and 19 are found by computing the nullspace of the matrix $\mathbf{Z}$ in Equations 7, 17, respectively. Figure 10 shows curves of neutral stability with thickened regions of each curve showing where the thrust is negative. Notice that no μ allows thrust-producing instability at $u_i = 0$. This is physically intuitive – after all, a flapping flag does not generate thrust! It is also interesting to note that systems with lower values of μ can produce thrust at lower u_i than high μ systems, though the higher mass systems have higher forward speed (u_e). It is important to remember, however, that merely having positive thrust from the tail does not guarantee that a given $u_i,\ u_e$ point can be reached. The system's drag and the thrust of the fluid jet will also govern the submersible's top speed. Since the drag of the system will, for a neutrally-buoyant vessel, be strongly related to the displacement and mass, we will reserve these concerns for a later work more closely tied to the physical realization of the submersible.

3.3 Hydrodynamic Efficiency

Similar to the expression for thrust, Equation 11 may be non-dimensionalized, and the average over one cycle computed, to give the average non-dimensional power W^*.

$$W^* = \frac{\overline{W} M_e^{1/2} L^3}{(EI)^{3/2}} = \frac{\omega_{cr}}{2\pi} \int_0^{\frac{2\pi}{\omega_{cr}}} \left(\left[\dot{Y}^2 \beta_e u_e - u_e^2 \beta_e^{1/2} Y' \dot{Y} \right]_{X=1} - \left[\dot{Y}^2 \beta_e u_e - u_e^2 \beta_e^{1/2} Y' \dot{Y} \right]_{X=0} \right) dT \tag{20}$$

The expression for efficiency is therefore

$$\eta = \frac{U_e \overline{\tau}}{\overline{W}} = \frac{U e \frac{\tau^* EI}{L^2}}{W^* \frac{(EI)^{3/2}}{M_e^{1/2} L^3}} = \frac{\tau^* u_e}{W^*} \tag{21}$$

Efficiencies computed via Equation 21 at various values of μ are given in Figure 11. Each curve considers the equation of motion when $u_i,\ u_e$ are such that the system is neutrally stable. Per the discussion in Wu [12], Equation 21 has meaning only when the thrust is positive. Figure 11 therefore only contains data at $u_i,\ u_e$ locations with positive thrust, the non-thickened portions of Figure 10. The flatness of the curves depicted in Figure 11 fits well with expectations about fish-like motion. That is, that the type of motions employed by fish are efficient over a broad range of swimming speeds. This broad peak is *not* characteristic of a typical marine propeller, which tends to be most efficient over a

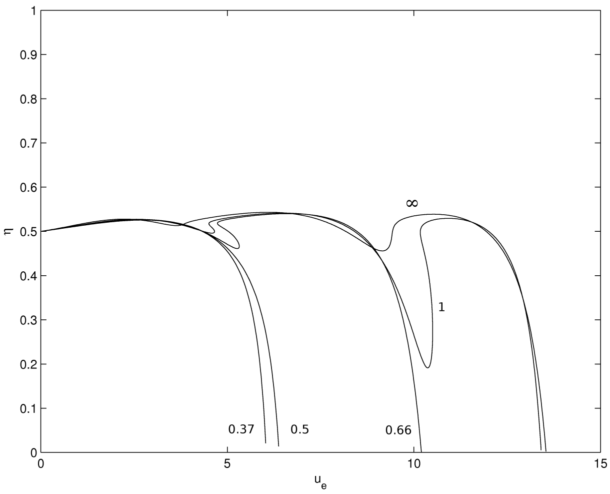

FIGURE 11. Curves of efficiency, η, for $\mu = 0.37,\ 0.5,\ 0.66,\ 1,\ \infty$. The waveforms used to compute efficiency are all taken from neutrally-stable, thrust-producing regions of Figure 10.

narrow range of velocities. It is interesting to note the collapse of the curves at low u_e; for $u_e < 4$, the efficiency is essentially the same for all values of μ. The curves' flatness and collapse is somewhat liberating from the standpoint of submersible design, since it means that the hull's mass can be chosen based on other needs, such as power source, drag, and buoyancy, rather than hydrodynamic efficiency.

4 Conclusion

The equations of motion for an immersed fluid-conveying pipe affixed to a rigid body have been derived, and the result compared to the classical [2] case of an immersed fluid-conveying cantilever. It was shown that both the cantilever and free pipe can be expressed as special cases of the rigid body boundary condition, as might be expected. It was found that as the mass of the rigid body (μ) decreases, the u_e required for instability at a given u_i decreases, though this is not a strong function of μ above $\mu \approx 1$. Estimates the sign of the thrust produced by the fluttering pipe and the efficiency of that thrust have also been computed. Regrettably, it is not possible to estimate the magnitude of the thrust without an estimate of the magnitude of the tail displacement such as might be gained through limit cycle analysis. We are therefore not able to compare the "fish-like" thrust of the fluttering tail to the "octopus-like" thrust of the jet on the basis of this work in its current form. In [3], also submitted to this Symposium, we present a more detailed (though analytically intractable) form of this work, and subject it to finite-difference simulation. It was found in that work that the speed of the submersible does increase as the magnitude of flutter increases, indicating a net increase in thrust. This is consistent with the findings of Paidoussis [5] in his original communication on the hydroelastic icthyoid propulsor. We also note that the efficiency of the produced thrust is relatively insensitive u_e over a large range of u_e. This is consistent with observations of live fish, which move with a waveform *reminiscent* of the travelling waveform generated by a fluid-conveying pipe, though not one we are able to reproduce in detail. It is therefore heartening that one of the great advantages of fish-like propulsion is preserved.

Acknowledgement

The support provided by the Office of Naval Research, ONR Grant Number N00014-08-1-0460, is gratefully acknowledged.

REFERENCES

[1] Rama B. Bhat and H. Wagner. Natural frequencies of a uniform cantilever with slender tip mass in the axial direction. *Journal of Sound and VIbration*, 46(2):304–307, 1976.

[2] M.J. Hannoyer and M.P. Paidoussis. Instabilities of tubular beams simultaneously subjected to internal and external axial flows. *ASME Journal of Mechanical Design*, 100:328–336, 1978.

[3] Mukherjee-R. Benard A. Hull A.J. Hellum, A.M. Dynamic modeling and simulation of a submersible propelled by a fluttering fluid conveying tail. In *3rd Joint US-European Fluids Engineering Summer Meeting*. ASME, August 2010.

[4] M.J. Lighthill. Note on the swimming of slender fish. *Journal of Fluid Mechanics*, 9:305–317, 1960.

[5] M.P. Paidoussis. Hydroelastic icthyoid propulsion. *AIAA Journal of Hydronautics*, 10:30–32, 1976.

[6] M.P. Paidoussis. Marine propulsion apparatus. US Patent 4,129,089, December 1978.

[7] M.P. Paidoussis. *Fluid-Structure Interactions: Slender Structures and Axial Flow, Volume 1*. Academic Press, 1998.

[8] M.P. Paidoussis. *Fluid-Structure Interactions: Slender Structures and Axial Flow, Volume 2*. Academic Press, 2004.

[9] M.P. Paidoussis and B.E. Laithier. Dynamics of timoshenko beams conveying fluid. *Journal of Mechanical Engineering Science*, 18:210–220, 1976.

[10] M. Potter and J. F. Foss. *Fluid Mechanics*. Great Lakes Press, 1982.

[11] Triantafyllou-G.S. Triantafyllou, M.S. and D.K.P. Yue. Hydrodynamics of fishlike swimming. *Annual Review of Fluid Mechanics*, 32:33–53, 2000.

[12] T. Yao-Tsu Wu. Hydromechanics of swimming propulsion. part 1. swimming and optimum movements of slennder fish with side fins. *Journal of Fluid Mechanics*, 46:545–568, 1971.